

# Structural phase transition, $s_{\pm}$ -wave pairing and magnetic stripe order in the bilayered nickelate superconductor $\text{La}_3\text{Ni}_2\text{O}_7$ under pressure

Yang Zhang,<sup>1</sup> Ling-Fang Lin,<sup>1</sup> Adriana Moreo,<sup>1,2</sup> Thomas A. Maier,<sup>3</sup> and Elbio Dagotto<sup>1,2</sup>

<sup>1</sup>*Department of Physics and Astronomy, University of Tennessee, Knoxville, Tennessee 37996, USA*

<sup>2</sup>*Materials Science and Technology Division, Oak Ridge National Laboratory, Oak Ridge, Tennessee 37831, USA*

<sup>3</sup>*Computational Sciences and Engineering Division, Oak Ridge National Laboratory, Oak Ridge, Tennessee 37831, USA*

Motivated by the recently discovered high-temperature superconductor  $\text{La}_3\text{Ni}_2\text{O}_7$  under pressure, we comprehensively study this system using density functional theory and the random phase approximation (RPA), focusing on pressure effects. At low pressures, the Amam phase is stable, containing the  $Y^{2-}$  mode distortion from the Fmmm phase, while the Fmmm phase is unstable. Because of small differences in enthalpy and a considerable  $Y^{2-}$  mode amplitude, the two phases may coexist in the range between 10.6 and 14 Gpa, beyond which the Fmmm phase dominates. In addition, our density functional theory and RPA calculations found that the magnetic stripe-type spin order with wavevector  $(\pi, 0)$  becomes stable at intermediate Hubbard and Hund couplings. Pairing is induced in the  $s_{\pm}$ -wave channel due to nesting between the  $\mathbf{M}=(\pi, \pi)$  and the  $\mathbf{X}=(\pi, 0)$  and  $\mathbf{Y}=(0, \pi)$  points in the Brillouin zone. This order resembles results for iron-based superconductors, but for the nickelate of our focus the orbital  $d_{3z^2-r^2}$  dominates, establishing a fundamental difference with iron pnictides and selenides. Within RPA, we predict that the critical temperature will substantially increase if the Fmmm phase is stabilized at lower pressures than currently achieved, via strain or growing on appropriate substrates, in agreement with tendencies in recent experimental results.

## Introduction

The recently discovered infinite-layer (IL) nickelate superconductors [1] opened the newest branch of the high-temperature superconductors family [2–7], including materials such as Sr-doped  $\text{RNiO}_2$  films ( $\text{R} = \text{Nd}$  or  $\text{Pr}$ ) [1, 8] and  $\text{Nd}_6\text{Ni}_5\text{O}_{12}$  [9]. Similar to the widely discussed high  $T_c$  cuprates superconductors [10, 11], the IL nickelates also have a  $d^9$  electronic configuration ( $\text{Ni}^{1+}$ ) in the parent phase, as well as a  $\text{NiO}_2$  two-dimensional (2D) square layer lattice. However, many theoretical and experimental efforts have revealed that “ $\text{Ni}^+$  is not  $\text{Cu}^{2+}$ ” [12], and the fundamental similarities and differences between individual IL nickelate and cuprates have been extensively discussed [7, 13–20]. One key difference is that in nickelates two  $d$ -orbitals ( $d_{3z^2-r^2}$  and  $d_{x^2-y^2}$ ) are important, while in cuprates only  $d_{x^2-y^2}$  is relevant.

Recently,  $\text{La}_3\text{Ni}_2\text{O}_7$  (LNO) (with the novel  $d^{7.5}$  configuration) was reported to be superconducting at high pressure, becoming the first non-IL  $\text{NiO}_2$  layered nickelate superconductor [21], with highest  $T_c \sim 80$  K. LNO displays the reduced Ruddlesden-Popper (RP) perovskite structure. At ambient conditions, LNO has the Amam structure with space group No. 63 [22], with an ( $a^-$ - $a^-$ - $c^0$ ) out-of-phase oxygen octahedral tilting distortion around the [110] axis from the  $I4/mmm$  phase [23]. By applying pressure of the order of 10 Gpa, the  $\text{NiO}_6$  rotations are suppressed and transform to an Fmmm space group (No. 69) [21]. Then, the Fmmm phase becomes superconducting in a broad pressure range from 14 to 43.5 Gpa [21].

Density functional theory (DFT) calculations revealed that the many components of the Fermi surface (FS) are contributed by the Ni orbitals  $d_{x^2-y^2}$  and  $d_{3z^2-r^2}$ . This FS consists of two-electron pockets with mixed  $e_g$  or-

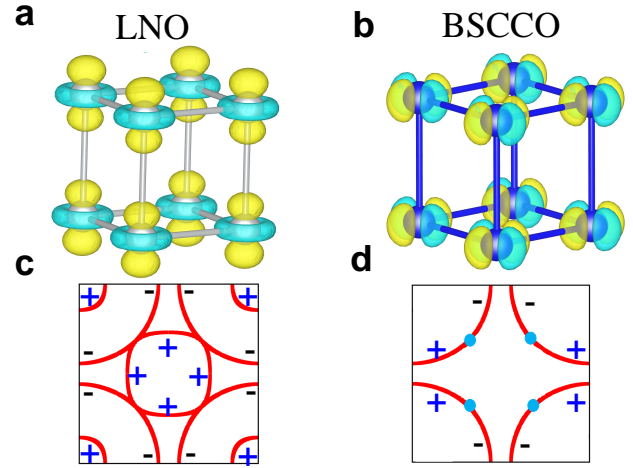


FIG. 1. **Differences between LNO and BSCCO.** **a** The dominant orbital  $d_{3z^2-r^2}$  of LNO vs. **b** the dominant orbital  $d_{x^2-y^2}$  of BSCCO. **c,d** Sketches of Fermi surfaces for LNO and BSCCO, including the signs of the superconducting order parameter.

bitals and a hole pocket dominated by the  $d_{3z^2-r^2}$  orbital, suggesting a Ni two-orbital minimum model is necessary [24, 25]. While completing our work, recent theoretical studies suggested that  $s_{\pm}$ -wave pairing superconductivity should dominate, in agreement with our results. This pairing channel is induced by spin fluctuations in the Fmmm phase of LNO [26–30], indicating also the importance of the  $d_{3z^2-r^2}$  orbital [24, 25, 31–33]. Furthermore, the role of the Hund coupling [25, 34], electronic correlation effects [31, 32, 35, 36], and the charge and spin instability [24, 33, 37] were also recently discussed.

Interestingly, the Amam to Fmmm phase transition

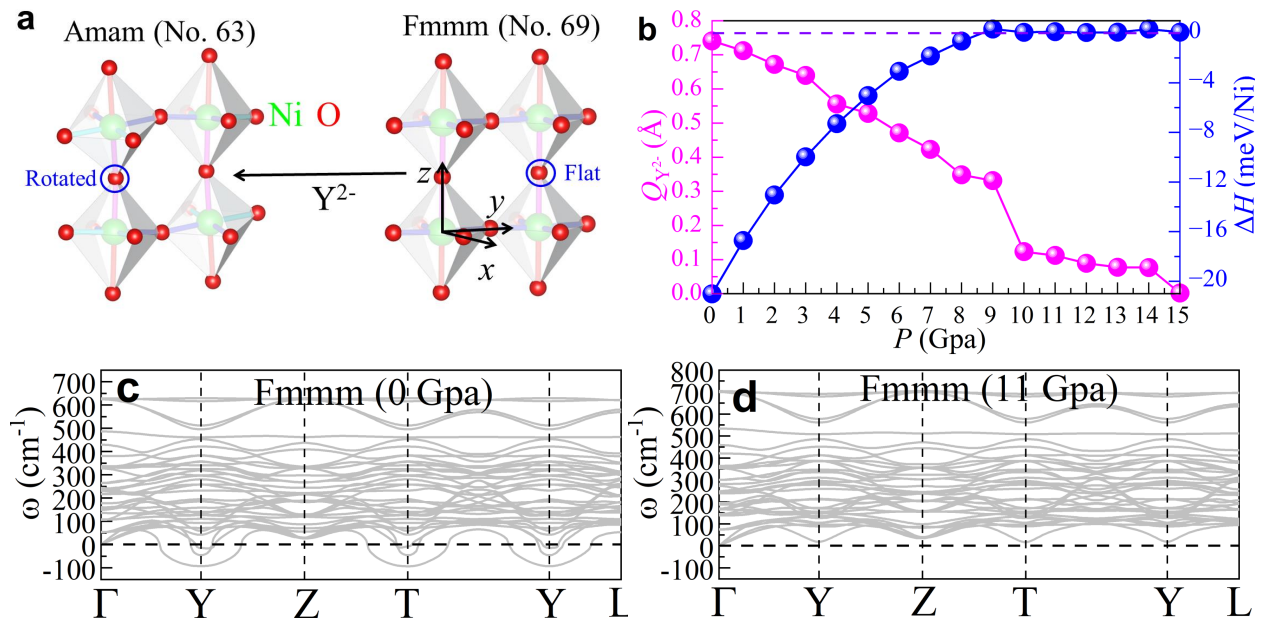


FIG. 2. **Crystal structures,  $Y^{2-}$  distortion amplitude, and phase transition.** **a** Schematic crystal structure of the bilayer  $NiO_6$  octahedron plane of LNO for the Amam (No. 63) and Fmmm (No. 69) phases (green = Ni; red = O), respectively. Different Ni-O bonds are distinguished by different colors. The local  $z$ -axis is perpendicular to the  $NiO_6$  plane towards the top O atom, while the local  $x$ - or  $y$ -axis is along the in-plane Ni-O bond directions. All crystal structures were visualized using the VESTA code [38]. **b** The  $Y^{2-}$  distortion amplitude and enthalpy ( $H = E + PV$ ) between the Amam and Fmmm phases [ $\Delta H = H(\text{Amam}) - H(\text{Fmmm})$ ] vs. pressure. Phonon spectrum of LNO for the **c** Fmmm (No. 69) phase at 0 Gpa, and **d** Fmmm (No. 69) phase at 11 Gpa, respectively. For the Fmmm phase, the coordinates of the high-symmetry points in the Brillouin zone (BZ) are  $\Gamma = (0, 0, 0)$ ,  $Y = (0.5, 0, 0.5)$ ,  $Z = (0.5, 0.5, 0)$ ,  $T = (0, 0.5, 0.5)$ , and  $L = (0.5, 0.5, 0.5)$ .

was found around 10 Gpa, but the superconductivity was obtained only above 14 Gpa [21]. In addition, the values of  $T_c$  do not dramatically change in a broad superconducting pressure region in the Fmmm phase of LNO [21]. In this case, several questions naturally arise for LNO: what interesting physics occurs between 10 to 14 Gpa? Why is the observed  $T_c$  in the superconducting pressure region 14 to 43.5 Gpa relatively independent of pressure, as opposed to showing a dome-like dependence? Are the Fmmm structure or pressure itself important for superconductivity? Does the FS topology and  $s_{\pm}$ -wave pairing symmetry change in the Fmmm phase under high pressure? What are the main differences between LNO and the previously well-studied bilayered system  $Bi_2Sr_2CaCu_2O_8$  (BSCCO) of the cuprate family?

To answer these questions, we studied in detail the LNO system under pressure, using first-principles DFT and random phase approximation (RPA) calculations. In the low-pressure region (0 to 10.5 Gpa), the Amam phase – with the  $Y^{2-}$  mode distortion from the Fmmm phase – is stable, while the Fmmm phase is unstable. Due to small differences in enthalpy and a considerable  $Y^{2-}$  mode amplitude, between 10.6 and 14 Gpa the Amam phase could potentially coexist with the Fmmm phase in the same sample, or leading to sample-dependent behavior, and resulting in a greatly reduced or vanishing  $T_c$  in this pressure region. Furthermore, in the range of pres-

ures studied, two pockets ( $\alpha$  and  $\beta$ ) with mixed  $d_{3z^2-r^2}$  and  $d_{x^2-y^2}$  orbitals, and a  $\gamma$  pocket made primarily of the  $d_{3z^2-r^2}$  orbital contribute to the FS. Compared to ambient pressure, the  $\gamma$  pocket is stretched and the  $\beta$  pocket is reduced in size. Furthermore, the DFT+ $U$  and RPA calculations suggest a stripe spin order instability with wavevector  $(\pi, 0)$ .

Thus, our results highlight that the main fundamental differences with BSCCO are: (i) in the Ni bilayer with two active Ni orbitals, it is  $d_{3z^2-r^2}$  that plays the key role, as compared to  $d_{x^2-y^2}$  for BSCCO cuprates (see sketch Fig. 1). (ii) This leads to  $s_{\pm}$ -wave pairing for Ni, while it is  $d$ -wave for Cu. Or, in other words, the inter-layer hybridization being large induces  $s_{\pm}$  in LNO, but when this hybridization is small then  $d$ -wave dominates as in cuprates. (iii) The FSs of LNO and BSCCO fundamentally differ with regards to the presence of hole pockets at  $(\pi, \pi)$  for LNO. These pockets are crucial for the stability of  $s_{\pm}$  pairing.

## Results

### DFT results

Based on the group analysis obtained from the AMPLIMODES software [39, 40], the distortion mode from the high symmetry phase (Fmmm) to the low symmetry phase (Amam) is the  $Y^{2-}$  (see Fig. 2a). At 0 Gpa,

the distortion amplitude of the  $Y^{2-}$  mode is  $\sim 0.7407$  Å. As shown in Fig. 2b, this  $Y^{2-}$  mode amplitude is gradually reduced under pressure, reaching nearly zero value at 15 Gpa ( $\sim 0.0016$  Å). At 0 Gpa, the Amam phase has an energy lower by about -21.01 meV/Ni than the Fmmm structure. As shown in Fig. 2b, the difference in enthalpy between the Amam and Fmmm phases also smoothly decreases by increasing pressure. Interestingly, the Fmmm and Amam phases have very close enthalpies in the pressure range from 9 to 14 Gpa, while the  $Y^{2-}$  mode distortion still exists with sizeable distortion amplitude in this region. To better understand the structural stability of LNO, we calculated the phonon spectrum of the Fmmm and Amam phases with or without pressure, by using the density functional perturbation theory approach [1, 42, 43] analyzed by the PHONOPY software [4, 5]. For the Amam phase of LNO, there is no imaginary frequency obtained in the phonon dispersion spectrum from 0 to 15 Gpa (see results in the Supplementary Note I), suggesting that the Amam phase is stable in this pressure range.

The phonon dispersion spectrum displays imaginary frequencies appearing at high symmetry points for the Fmmm structure of LNO below 10.5 Gpa (see the results of 0 Gpa as example, in Fig. 2c). However, the Fmmm phase becomes stable without any imaginary frequency from 10.6 Gpa to 50 Gpa, the maximum value we studied (see  $P = 11$  Gpa as an example in Fig. 2d, while the rest of the results can be found in the Supplementary Note I). Between 10.6 and 14 Gpa, Fmmm has an enthalpy slightly lower than that of the Amam state ( $< \sim 0.3$  meV/Ni). This value ( $\sim 10.6$  Gpa) is quite close to the experimental observed critical pressure ( $\sim 10$  Gpa) for the Amam to Fmmm transition [21].

Recent DFT calculations found that the pocket around  $(\pi, \pi)$  vanishes in the Amam phase [21]. This pocket induces the  $s_{\pm}$ -wave pairing symmetry in the superconducting phase, as discussed below. Due to the small difference in enthalpy and considerable  $Y^{2-}$  mode amplitude in this pressure range, the Amam phase could also be obtained experimentally in some portions of the same sample of LNO. Recent experiments also suggest a first-order structural transition from the Amam to Fmmm phases under pressure [21]. In this case, the  $T_c$  would be greatly reduced or vanish in this pressure region due to the coexistence with the Amam phase, leading to sample-dependent behavior.

While finishing the present manuscript, we noted that a very recent experimental effort reported zero resistance below 10 K in some samples above 10 Gpa and below 15 Gpa [46], supporting our conclusion. This could also qualitatively explain the absence of superconductivity between 10 and 14 Gpa in the original high-pressure efforts [21]. At 15 Gpa, our DFT results found that the  $Y^{2-}$  mode amplitude is almost zero ( $\sim 0.0016$  Å), indicating a pure Fmmm symmetry phase and robust superconductivity above 15 Gpa.

### Tight-binding results

Next, we constructed a four-band  $e_g$  orbital tight binding (TB) model in a bilayer lattice [47–51] for the Fmmm phase. It is four orbitals because the unit cell contains two Ni's, and each Ni contributes two orbitals. As pressure increases, the values of the hopping matrix elements also increase. As shown in Fig. 3 a, the ratio of  $t_{11}^z$  ( $d_{3z^2-r^2}$  along the inter-layer direction) and  $t_{22}^{x/y}$  ( $d_{x^2-y^2}$  in plane) slightly decreases from 1.325 (0 Gpa) to 1.309 (29.5 Gpa) and further to 1.286 (50 Gpa), although with some small oscillations. Furthermore, the in-plane  $|t_{12}/t_{22}|$  increases from 0.457 (0 Gpa) to 0.483 (50 Gpa), suggesting an enhanced hybridization between  $d_{3z^2-r^2}$  and  $d_{x^2-y^2}$  orbitals under pressure (see Fig. 3 b). Moreover, the crystal field splitting  $\Delta$  also increases under pressure, with small oscillations, as displayed in Fig. 3 c. These small oscillations may be caused by a lack of convergence of optimized crystal structures at some pressure values, but do not change the main physical conclusions discussed in our publication.

The TB calculations indicate that the electronic density of the  $d_{3z^2-r^2}$  orbital gradually reduces from 1.86 (0 Gpa) to 1.78 (50 Gpa), as shown in Fig. 3 d. Note that the electronic population of both orbitals is not an integer, thus this system is “self-doped”. The band structures indicate that the bandwidth of  $e_g$  orbitals increases by about  $\sim 23.1\%$ , from 0 ( $\sim 3.63$  eV) to 50 ( $\sim 4.47$  eV) Gpa (see Figs. 3 e and f). Furthermore, the  $e_g$  states of Ni display the orbital-selective spin singlet formation behavior [25], where the energy gap  $\Delta E$  between bonding and antibonding states of the  $d_{3z^2-r^2}$  orbital increases by about 20% from 0 Gpa ( $\sim 1.20$  eV) to 50 Gpa ( $\sim 1.44$  eV).

In addition, a van Hove singularity (vHS) near the Fermi level was also found at the  $X$  point  $(\pi, 0)$  in the BZ (see Figs. 3 e and f), indicating a possible stripe  $(\pi, 0)$  order instability. As pressure increases, the vHS shifts away from the Fermi level, leading to reduced magnetic scattering near  $(\pi, 0)$ , as discussed in the following section. The FS consists of two electron pockets ( $\alpha$  and  $\beta$ ) with a mixture of  $d_{3z^2-r^2}$  and  $d_{x^2-y^2}$  orbitals, while the  $\gamma$  hole-pocket is made up almost exclusively of the  $d_{3z^2-r^2}$  orbital at all pressures we studied (see  $P = 0$  and 50 Gpa as examples in Figs. 3 g and h, and the Supplementary Note II for other pressures). The  $\gamma$  pocket increases in size with pressure, while the size of the  $\beta$  pocket decreases at high pressure.

### Stripe order instability

As displayed in Figs. 4 a and b, the stripe  $(\pi, 0)$  magnetic order has the lowest energy among the three magnetic candidates considered in the pressure region that we studied, using robust Hund couplings  $J = 0.8$  eV and  $J = 1.0$  eV. Furthermore, the energy differences between the stripe and other magnetic configurations decreases as the pressure increases. By reducing  $J$  to 0.6 eV (see Fig. 4 c), the stripe order  $(\pi, 0)$  has the lowest energy below 25 Gpa, while it has a close energy ( $\sim 0.3$  meV/Ni) to the

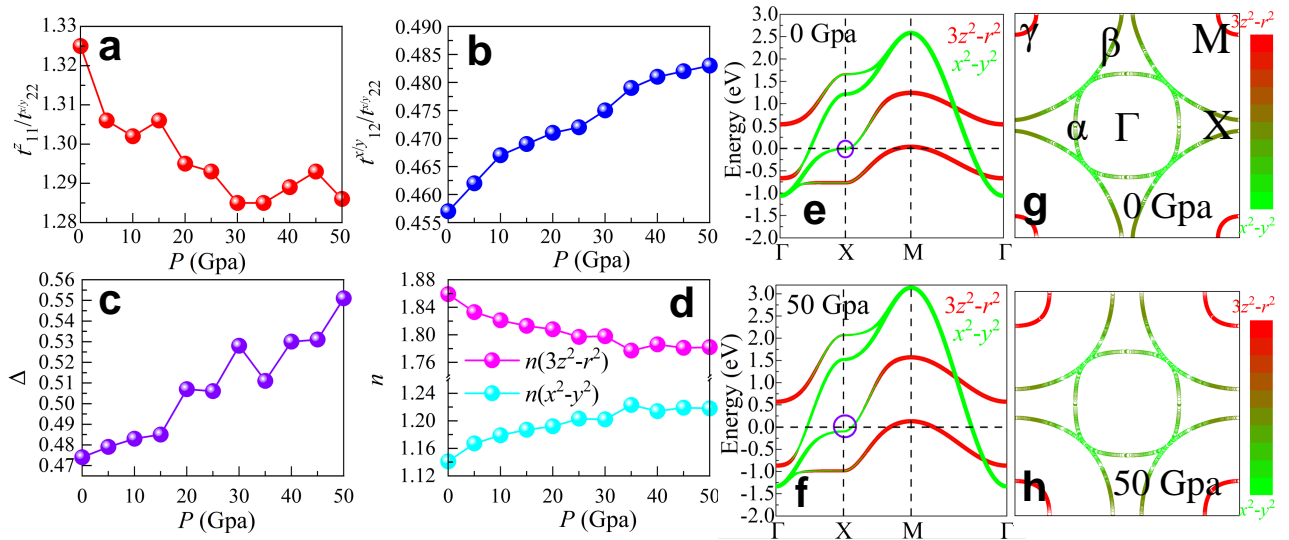


FIG. 3. **TB results.** **a** Ratio of hoppings  $t_{11}^z/t_{22}^{x/y}$ , **b** ratio of hoppings  $t_{12}^{x/y}/t_{22}^{x/y}$ , **c** crystal-field splitting  $\Delta$ , and **d** electronic density  $n$ , vs. pressure. The  $\gamma = 1$  and  $\gamma = 2$  orbitals correspond to the  $d_{3z^2-r^2}$  and  $d_{x^2-y^2}$  orbitals, respectively. **e-f** Band structures and **g-h** FSs for 0 and 50 GPa, respectively. Here, the four-band  $e_g$  orbital TB model was considered with the nearest-neighbor (NN) hoppings in a bilayer lattice for the overall filling  $n = 3$  (1.5 electrons per site). Furthermore, the vHS near the X point is also marked by purple circles. The NN hoppings and crystal field  $\Delta$ s are obtained from the maximally localized Wannier functions [6] by fitting DFT and Wannier bands for different pressures. The hoppings and crystal-field splitting  $\Delta$  used at 0 GPa are:  $t_{11}^x = t_{11}^y = -0.088$ ,  $t_{12}^x = 0.208$ ,  $t_{12}^y = -0.208$ ,  $t_{22}^x = t_{22}^y = -0.455$ ,  $t_{11}^z = -0.603$ , and  $\Delta = 0.474$ . The hoppings and crystal-field splitting  $\Delta$  used at 50 GPa are:  $t_{11}^x = t_{11}^y = -0.125$ ,  $t_{12}^x = 0.270$ ,  $t_{12}^y = -0.270$ ,  $t_{22}^x = t_{22}^y = -0.559$ ,  $t_{11}^z = -0.719$ , and  $\Delta = 0.551$ . All the hoppings and crystal-field splitting are in eV units. The coordinates of the high-symmetry points in the BZ are  $\Gamma = (0, 0)$ ,  $X = (0.5, 0)$ , and  $M = (0.5, 0.5)$ .

G-AFM phase above 25 GPa, suggesting the important role of  $J$  to stabilize stripe order. Under pressure, the intraorbital hopping of the  $e_g$  orbitals increases, enhancing the canonical antiferromagnetic (AFM) Heisenberg interaction. Furthermore, the reduced  $J$  would also reduce the ferromagnetic (FM) coupling caused by the interorbital hopping between half-filled and empty orbitals via Hund’s coupling  $J$  [25, 54]. If continuing to reduce  $J$ , then the AFM Heisenberg interaction induced by the intraorbital hopping will eventually win, leading to G-type AFM order (see the results for  $J = 0.4$  eV in Supplementary Note III).

Considering quantum fluctuations, the system may not develop long-range order due to the in-plane AFM and FM competition in portions of the vast parameter space involving hoppings, Hund coupling  $J$ , and Hubbard interaction  $U$ . This competition deserves further many-body model studies. In addition, the calculated magnetic moment of the magnetic stripe phase also decreases under pressure (Fig. 4 d) because increasing the hoppings (namely, increasing the bandwidth  $W$ ) “effectively” reduces the electronic correlation via  $U/W$ . Finally, note that the stripe order  $(\pi, 0)$  is degenerate with stripe order  $(0, \pi)$ . Thus, there could occur an Ising spontaneous symmetry breaking upon cooling before long-range order is reached. Consequently, these results predict the existence of “nematicity” in LNO above the Néel temperature, as it occurs in iron-based superconductors [55, 56].

To assess the DFT extracted TB models for their magnetic and superconducting behavior, we have performed multi-orbital RPA calculations (see Methods section) for the Fmmm phase of LNO. Figure 5 shows the static RPA enhanced spin susceptibility  $\chi'(\mathbf{q}, \omega = 0)$  for  $q_z = \pi$  and  $q_x, q_y$  along a high-symmetry path in the Brillouin zone. Consistent with the DFT results, at 0 GPa,  $\chi'(\mathbf{q}, \omega = 0)$  has a strong peak near the stripe wavevector  $\mathbf{q} = (\pi, 0)$ . A closer inspection of the contributions to the spin susceptibility (not shown) shows that the dominant scattering process giving rise to this peak comes from intra-orbital  $d_{3z^2-r^2}$  scattering between the  $(0, \pi)$  region on the  $\beta$  electron pocket and the  $\gamma$  hole pocket at  $(\pi, \pi)$ .

This strong enhancement of the magnetic scattering at this wavevector can be understood from the bandstructure shown in panel e of Fig. 3. The band that gives rise to the  $\beta$  sheet has a saddle-point at  $(\pi, 0)$  right at the Fermi level for 0 GPa, leading to a vHS in the density of states and therefore increased scattering. For larger pressures, this saddle-point moves away from the Fermi level (see Fig. 3 f), and, as a consequence, the magnetic scattering near  $(\pi, 0)$  is reduced, as shown in Fig. 5. This is also in agreement with the decreasing energy differences between Stripe  $(\pi, 0)$  and other magnetic states under pressures obtained from DFT+ $U$  calculations (see Fig. 4). Furthermore, the huge reduction of magnetic scattering under pressure also suggests the long-range spin stripe order may not be stable at high pressure.

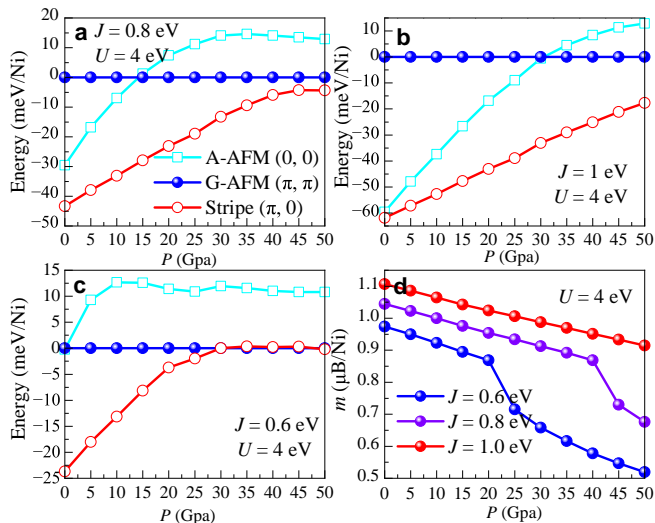


FIG. 4. **Magnetic results.** The DFT+ $U+J$  calculated energies for **a**  $J = 0.8$  eV, **b**  $J = 1$  eV, and **c**  $J = 0.6$  eV of different magnetic configurations vs different values of pressure for the Fmmm phase of LNO, all at  $U = 4$  eV, respectively, taking the G-AFM state as zero of reference. **d** The calculated magnetic moment of the stripe  $(\pi, 0)$  magnetic order for different values of  $J$ , at  $U = 4$  eV. To better understand the Hund coupling role,  $J$  was changed from 0.6 to 1.0 eV by fixing  $U = 4$  eV [21, 32, 37, 53]. Here, we also studied three possible in-plane spin orders: A-AFM with  $(0, 0)$ , G-AFM with  $(\pi, \pi)$ , and stripe  $(\pi, 0)$  using the optimized crystal structures at different pressures. The magnetic coupling between layers was considered to be AFM in all cases. The differences in total energy and enthalpy between different magnetic configurations are the same due to the same crystal structures at different pressures.

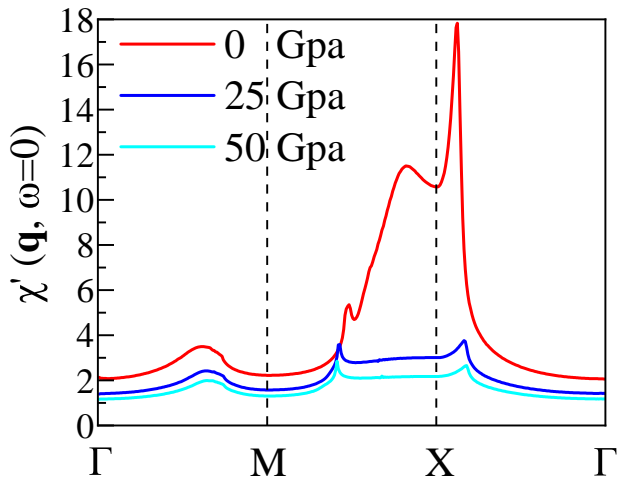


FIG. 5. **RPA magnetic susceptibility.** The RPA calculated static spin susceptibility  $\chi'(\mathbf{q}, \omega = 0)$  versus  $q_x, q_y$  for  $q_z = \pi$  for the two-orbital bilayer TB model for three different pressures. At 0 GPa,  $\chi'(\mathbf{q}, \omega = 0)$  shows a strong peak at  $\mathbf{q} = (\pi, 0)$  (and symmetry related wavevectors), which is suppressed at higher pressure. Here we used  $U = 0.8$ ,  $U' = 0.4$ ,  $J = J' = 0.2$  in units of eV. All hoppings and crystal fields are for the Fmmm phase.

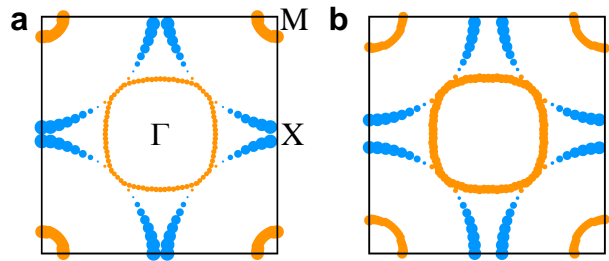


FIG. 6. **Leading RPA gap structure.** The RPA calculated leading superconducting gap structure  $g_\alpha(\mathbf{k})$  for momenta  $\mathbf{k}$  on the FS for **a** 0 GPa and **b** 25 GPa has  $s^\pm$  symmetry, where the gap changes sign between the  $\alpha$  and  $\beta$  FS pockets, and also between the  $\beta$  and  $\gamma$  pockets. The sign of the gap is indicated by color (orange = positive, blue = negative), and gap amplitude by thickness. With increasing pressure, the gap amplitude on the  $\alpha$  pocket grows relative to that on the  $\beta$  and  $\gamma$  pockets. Independent of pressure, the gap on the  $\beta$  pocket is very small and has nodal points near the zone diagonal. Hoppings and crystal fields are for the Fmmm phase.

### Pairing symmetry

In the RPA approach, the spin (and also charge) susceptibilities enter directly in the pairing interaction for the states on the FS. Figure 6 displays the leading pairing symmetry  $g_\alpha(\mathbf{k})$  obtained from solving the eigenvalue problem in Eq. (2) (Methods section) for the RPA pairing interaction for the model at (a) 0 GPa and (b) 25 GPa. In both cases, the leading superconducting gap has an  $s^\pm$  structure, where the gap switches sign between the  $\alpha$  and  $\beta$  pockets, and between the  $\beta$  and  $\gamma$  pockets. As for the spin susceptibility, and as one would expect for spin-fluctuation mediated pairing, a detailed analysis of the different contributions to the  $s^\pm$  pairing strength reveals that this gap structure is driven by intra-orbital  $(\pi, 0)$  scattering between the  $(0, \pi)$  region of the  $\beta$ -sheet with significant  $d_{3z^2-r^2}$  character of the Bloch states, to the  $d_{3z^2-r^2}$   $\gamma$ -pocket at  $(\pi, \pi)$ . Moreover, the gap amplitude on the  $\alpha$  pocket grows relative to that on the  $\beta$  and  $\gamma$  pockets with increasing pressure. Also, independent of pressure, the gap on the  $\beta$  pocket has strong momentum dependence, becoming very small near the zone diagonal where it has accidental nodes. We reserve a detailed analysis of the factors leading to this momentum dependence for a future study.

Finally, we show in Fig. 7 the pressure dependence of the pairing strength  $\lambda$  of the leading  $s^\pm$  gap. The  $s^\pm$  gap remains the leading instability over the subleading  $d_{x^2-y^2}$  gap over the entire pressure range we considered. With increasing pressure, both pairing strengths monotonically decrease. This decrease is explained by the decrease in  $(\pi, 0)$  scattering in the spin susceptibility shown in Fig. 5 with increasing pressure, and therefore can again be traced to the pressure evolution of the bandstructure shown in Fig. 3. In the RPA approach

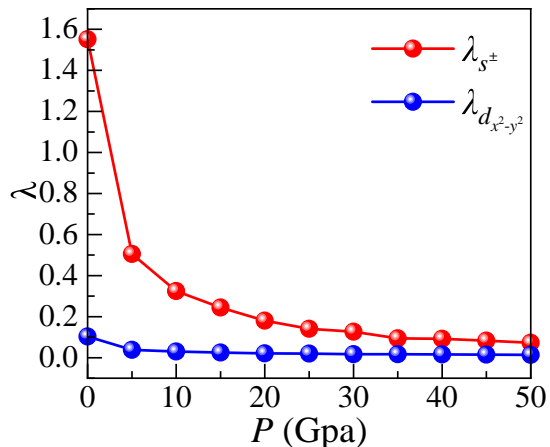


FIG. 7. **Pressure dependence of leading pairing strength.** The RPA calculated pairing strength  $\lambda$  for the leading  $s^\pm$  and subleading  $d_{x^2-y^2}$  instabilities versus pressure for the pressure dependent bilayer model with  $U = 0.8$ ,  $U' = 0.4$ ,  $J = J' = 0.2$ . The  $s^\pm$  instability is leading over the full pressure range and its pairing strength increases monotonically with decreasing pressure. All hoppings and crystal fields are for the Fmmm phase.

we use, changes in the pairing strength  $\lambda$  translate to changes in the superconducting transition temperature  $T_c$  through a Bardeen-Cooper-Schrieffer (BCS) like equation,  $T_c = \omega_0 e^{-1/\lambda}$ , where  $\omega_0$  is a cut-off frequency that is determined from the spin-fluctuation spectrum.

We also performed additional calculations for a model with artificially large crystal-field splitting  $\Delta = 0.6$  eV at 0 GPa, for which the hole band sinks below the Fermi level and the  $\gamma$ -pocket disappears (see the results in Supplementary Note IV). For this case,  $\lambda_{s^\pm}$  is suppressed significantly from 1.55 (at  $\Delta = 0.474$ ) to 0.040, and  $\lambda_{d_{x^2-y^2}}$  becomes the leading solution, albeit with a similarly small  $\lambda_{d_{x^2-y^2}} = 0.045$ . Consistent with the discussion above, this provides further evidence of the importance of the  $(\pi, \pi)$   $\gamma$  hole pocket in mediating superconductivity in this system. This could explain the absence of superconductivity in the low-pressure Amam phase of LNO [21], where the  $\gamma$  pocket around  $(\pi, \pi)$  vanishes, indicating the importance of the Fmmm phase for the superconductivity in LNO system.

## Discussion

The recently discovered bilayer nickelate superconductor LNO has opened a new platform for the study of the origin of unconventional superconductivity, unveiling several challenging results that theory needs to explain. Combining first-principles DFT and many-body RPA methods, here we comprehensively studied the LNO system under pressure from  $P = 0$  GPa to  $P = 50$  GPa. Based on group analysis, the distortion  $Y^{2-}$  mode induces the structural transition from Fmmm (No. 69) to Amam (No. 63). At 0 GPa, the Amam phase has lower

energy ( $\sim -21.01$  meV/Ni) than the Fmmm phase due to a large distortion amplitude of  $Y^{2-}$  mode ( $\sim 0.7407$  Å). By introducing pressure, the  $Y^{2-}$  mode amplitude is gradually reduced, reaching nearly zero value at 15 GPa ( $\sim 0.0016$  Å), while the enthalpy difference [ $\Delta H = H(\text{Amam}) - H(\text{Fmmm})$ ] also decreases. Furthermore, there is no imaginary frequency obtained for the Amam structure from 0 to 15 GPa. The Fmmm phase eventually becomes stable at  $\sim 10.6$  GPa, which is quite close to the experimentally observed critical pressure ( $\sim 10$  GPa) of the Fmmm structure of LNO.

In the pressure range from 10.6 to 14 GPa, we found that the enthalpy differences between the Amam and Fmmm phases are quite small ( $\sim 0.3$  meV/Ni), while the  $Y^{2-}$  mode amplitude is still considerable ( $\sim 0.1$  Å). Furthermore, both the Amam and Fmmm phases are stable in this pressure region. In this case, the Amam phase could coexist with the Fmmm phase in samples of LNO, suggesting a first-order pressure-induced structural phase transition from Amam to Fmmm. Due to the existence of the Amam phase in the Fmmm structure of the LNO sample, as an overall effect the superconducting  $T_c$  would be gradually reduced or fully vanish in the intermediate pressure region, leading to potentially sample-dependent issues, supporting recent experiments where zero resistance was found below 10 K in some samples above 10 GPa and below 15 GPa [46]. This could qualitatively explain the absence of superconductivity in LNO for the Fmmm structure in the pressure region from 10 to 14 GPa [21]. More detailed studies are needed to confirm our results and obtain direct experimental evidence for the coexistence of the Amam and Fmmm phases in this pressure region.

Furthermore, a vHs near the Fermi level was found at the  $X(\pi, 0)$  point in the BZ in our TB band structure, indicating a possible stripe  $(\pi, 0)$  order instability. Our DFT+ $U+J$  and RPA results both indicate that the magnetic stripe phase with wavevector  $(\pi, 0)$  [degenerate with  $(0, \pi)$ ] should dominate once Hubbard and Hund correlation effects are taken into account, at least in the intermediate range of Hubbard-Hund couplings. Moreover, due to the particular shape of the FS, and its orbital composition, the  $s^\pm$  pairing channel should be the pairing symmetry of LNO. Note that Fig. 7, with a rapidly increasing  $\lambda$  for  $s^\pm$  as pressure is reduced, strongly suggests that the critical temperature will considerably increase from the current record of 80 K if the Fmmm phase could be made stable at ambient pressure, perhaps via strain or by growing LNO over appropriate substrates that suppress the competing Amam state.

The significant suppression of the  $s^\pm$  pairing strength we find in calculations without the  $\gamma$  pocket provide strong evidence of the importance of the  $(\pi, \pi)$   $\gamma$  hole pocket in mediating superconductivity in this system. This could also explain why superconductivity is only observed in the high-pressure Fmmm phase since the  $\gamma$  hole pocket around  $(\pi, \pi)$  vanishes in the Amam phase, suggesting the importance of the Fmmm phase (stable  $\gamma$

pocket) for superconductivity in the LNO system.

## Methods

### DFT method

In this work, first-principles DFT calculations were implemented based on the Vienna *ab initio* simulation package (VASP) code, by using the projector augmented wave (PAW) method [57–59]. The electronic correlations were considered by the generalized gradient approximation and the Perdew-Burke-Ernzerhof exchange potential [60]. The plane-wave cutoff energy was set as 550 eV and a  $k$ -point grid  $12 \times 12 \times 3$  was adopted for the conventional structure of LNO of both the Amam and Fmmm phases. Note we also tested that this  $k$ -point mesh produces converged energies. Moreover, the lattice constants and atomic positions were fully relaxed until the Hellman-Feynman force on each atom was smaller than 0.01 eV/Å. Moreover, the onsite Coulomb interactions were considered via the Dudarev formulation [61] with  $U_{eff} = 4$  eV in the relation of crystal structures under pressure, as used in recent studies of LNO [21, 32, 37].

We calculated the phonon spectra of the Amam and Fmmm phases for different pressures by using the density functional perturbation theory approach [1, 42, 43], analyzed by the PHONOPY software in the primitive unit cell [4, 5]. We chose the conventional cell structures, corresponding to the  $\sqrt{2} \times \sqrt{2} \times 1$  supercell of the undistorted parent  $I4/mmm$  conventional cell, to study the dynamic stability, which is enough to obtain possible unstable modes for the 327-type RP perovskite system. In addition to the standard DFT calculation discussed thus far, the maximally localized Wannier functions (MLWFs) method was employed to fit Ni's  $e_g$  bands and obtain the hoppings and crystal-field splitting for model calculations, by using the WANNIER90 packages [6].

### TB method

In our TB model, a four-band bilayer lattice with filling  $n = 3$  was used, corresponding to 1.5 electrons per site, where the kinetic hopping component is:

$$H_k = \sum_{\substack{i\sigma \\ \vec{\alpha}\gamma\gamma'}} t_{\gamma\gamma'}^{\vec{\alpha}} (c_{i\sigma\gamma}^\dagger c_{i+\vec{\alpha}\sigma\gamma'} + H.c.) + \sum_{i\gamma\sigma} \Delta_\gamma n_{i\gamma\sigma}. \quad (1)$$

The first term represents the hopping of an electron from

orbital  $\gamma$  at site  $i$  to orbital  $\gamma'$  at the nearest-neighbor (NN) site  $i + \vec{\alpha}$ .  $c_{i\sigma\gamma}^\dagger (c_{i\sigma\gamma})$  is the standard creation (annihilation) operator,  $\gamma$  and  $\gamma'$  represent the different orbitals, and  $\sigma$  is the  $z$ -axis spin projection.  $\Delta_\gamma$  represents the crystal-field splitting of each orbital  $\gamma$ . The unit vectors  $\vec{\alpha}$  are along the three directions.

The NN hopping matrix of different pressures was obtained from MLWFs. The detailed values can be found in Supplementary Note II. The Fermi energy is obtained by integrating the density of states for all  $\omega$  to count the number of electrons  $n = 3$ . Based on the obtained Fermi energy, a  $4000 \times 4000$  k-mesh was used to calculate the FS.

### RPA calculations

The RPA method we used to assess the bilayer TB models for their magnetic and superconducting behavior is based on a perturbative weak-coupling expansion in the Coulomb interaction. It has been shown in many studies to capture the essence of the physics (e.g. Ref. [62]). In the multi-orbital RPA approach [63–65], the RPA enhanced spin susceptibility shown in Fig. 5 is obtained from the bare susceptibility (Lindhart function)  $\chi_0(\mathbf{q})$  as  $\chi(\mathbf{q}) = \chi_0(\mathbf{q})[1 - \mathcal{U}\chi_0(\mathbf{q})]^{-1}$ . Here,  $\chi_0(\mathbf{q})$  is an orbital-dependent susceptibility tensor and  $\mathcal{U}$  is a tensor that contains the intra-orbital  $U$  and inter-orbital  $U'$  density-density interactions, the Hund's rule coupling  $J$ , and the pair-hopping  $J'$  term. The pairing strength  $\lambda_\alpha$  for channel  $\alpha$  shown in Fig. 7 and the corresponding gap structure  $g_\alpha(\mathbf{k})$  shown in Fig. 6 are obtained from solving an eigenvalue problem of the form

$$\int_{FS} d\mathbf{k}' \Gamma(\mathbf{k} - \mathbf{k}') g_\alpha(\mathbf{k}') = \lambda_\alpha g_\alpha(\mathbf{k}), \quad (2)$$

where the momenta  $\mathbf{k}$  and  $\mathbf{k}'$  are on the FS and  $\Gamma(\mathbf{k} - \mathbf{k}')$  contains the irreducible particle-particle vertex. In the RPA approximation, the dominant term entering  $\Gamma(\mathbf{k} - \mathbf{k}')$  is the RPA spin susceptibility  $\chi(\mathbf{k} - \mathbf{k}')$ . For the models considered here, we find that the eigenvector  $g_\alpha(\mathbf{k})$  corresponding to the largest eigenvalue  $\lambda_\alpha$  has  $s^\pm$  symmetry as shown in Fig. 6. More details of the multi-orbital RPA approach can be found in [63–66].

### Data availability

The data that support the findings of this study are available from the corresponding author upon request.

- 
- [1] Li, D. *et al.* Superconductivity in an infinite-layer nickelate *Nature* **572**, 624 (2019).
- [2] Nomura, Y. *et al.* Formation of a two-dimensional single-component correlated electron system and band engineering in the nickelate superconductor NdNiO<sub>2</sub> *Phys. Rev. B* **100**, 205138 (2019).
- [3] Botana, A. S., & Norman, M. R. Similarities and Differences between LaNiO<sub>2</sub> and CaCuO<sub>2</sub> and Implications for Superconductivity *Phys. Rev. X* **10**, 011024 (2020).
- [4] Nomura, Y. & Arita, R. Superconductivity in infinite-layer nickelates *Rep. Prog. Phys.* **85**, 052501 (2022).
- [5] Zhou, X. Experimental progress on the emergent infinite-layer Ni-based superconductor *Materials Today* **55**, 170 (2022).
- [6] Gu, Q. & Wen, W.-H. Superconductivity in nickel-based 112 systems *Innovation* **3**, 100202 (2022).
- [7] Zhang, Y. *et al.* Similarities and differences between nickelate and cuprate films grown on a SrTiO<sub>3</sub> substrate *Phys.*

- Rev. B* **102**, 195117 (2020).
- [8] Zeng, S. *et al.* Phase Diagram and Superconducting Dome of Infinite-Layer  $\text{Nd}_{1-x}\text{Sr}_x\text{NiO}_2$  Thin Films *Phys. Rev. Lett.* **125**, 147003 (2020).
- [9] Pan, G. A. *et al.* Superconductivity in a quintuple-layer square-planar nickelate *Nat. Mater.* **21**, 160 (2022).
- [10] Bednorz, J. G. & Müller, K. A. Possible high  $T_c$  superconductivity in the Ba-La-Cu-O system *Z. Phys. B: Condens. Matter* **64**, 189 (1986).
- [11] Dagotto, E. Correlated electrons in high-temperature superconductors. *Rev. Mod. Phys.* **66**, 763 (1994).
- [12] Lee, K.-W. & Pickett, W. E. Infinite-layer  $\text{LaNiO}_2$ :  $\text{Ni}^{1+}$  is not  $\text{Cu}^{2+}$  *Phys. Rev. B* **70**, 165109 (2004).
- [13] Sakakibara, H. *et al.* Model Construction and a Possibility of Cupratelike Pairing in a New  $d^9$  Nickelate Superconductor  $(\text{Nd,Sr})\text{NiO}_2$  *Phys. Rev. Lett.* **125**, 077003 (2020).
- [14] Jiang, M., Berciu, M. & Sawatzky G. A. Critical Nature of the Ni Spin State in Doped  $\text{NdNiO}_2$  *Phys. Rev. Lett.* **124**, 207004 (2020).
- [15] Wu, X. *et al.* Robust  $d_{x^2-y^2}$ -wave superconductivity of infinite-layer nickelates *Phys. Rev. B* **101**, 060504(R) (2020).
- [16] Werner, P. & Hoshino, S. Nickelate superconductors: Multiorbital nature and spin freezing *Phys. Rev. B* **101**, 041104(R) (2020).
- [17] Gu, Y., Zhu, S., Wang, X., Hu, J. & Chen, H. A substantial hybridization between correlated Ni-d orbital and itinerant electrons in infinite-layer nickelates *Commun. Phys.* **3**, 84 (2020).
- [18] Karp, J. *et al.* Many-Body Electronic Structure of  $\text{NdNiO}_2$  and  $\text{CaCuO}_2$  *Phys. Rev. X* **10**, 021061 (2020).
- [19] Fowlie, M. *et al.* Intrinsic magnetism in superconducting infinite-layer nickelates *Nat. Phys.* **18**, 1043 (2022).
- [20] Rossi, M. *et al.* A broken translational symmetry state in an infinite-layer nickelate *Nat. Phys.* **18**, 869 (2022).
- [21] Sun, H. *et al.* Signatures of superconductivity near 80 K in a nickelate under high pressure *Nature* (2023).
- [22] Ling, C. D., Argyriou, D. N., Wu, G. & Neumeier, Neutron Diffraction Study of  $\text{La}_3\text{Ni}_2\text{O}_7$ : Structural Relationships Among  $n = 1, 2$ , and 3 Phases  $\text{La}_{n+1}\text{Ni}_n\text{O}_{3n+1}$  *J. Solid State Chem.* **152** 517 (2000).
- [23] Zhang, Z., Greenblatt, M. & Goodenough, J. B. Synthesis, Structure, and Properties of the Layered Perovskite  $\text{La}_3\text{Ni}_2\text{O}_7 - \delta$  *J. Solid State Chem.* **108** 402 (1994).
- [24] Luo, Z., Hu, X., Wang, M., Wu, W. & Yao, D.-X. Bilayer two-orbital model of  $\text{La}_3\text{Ni}_2\text{O}_7$  under pressure *arXiv* 2305.15564 (2023).
- [25] Zhang, Y., Lin, L.-F., Moreo, A. & Dagotto, E. Electronic structure, orbital-selective behavior, and magnetic tendencies in the bilayer nickelate superconductor  $\text{La}_3\text{Ni}_2\text{O}_7$  under pressure *arXiv* 2306.03231 (2023).
- [26] Yang, Q.-G., Wang, D. & Wang, Q.-H. Possible  $s_{\pm}$ -wave superconductivity in  $\text{La}_3\text{Ni}_2\text{O}_7$  *arXiv* 2306.03706 (2023).
- [27] Sakakibara, H., Kitamine, N., Ochi, M. & Kuroki, K. Possible high  $T_c$  superconductivity in  $\text{La}_3\text{Ni}_2\text{O}_7$  under high pressure through manifestation of a nearly-half-filled bilayer Hubbard model *arXiv* 2306.06039 (2023).
- [28] Gu, Y., Le, C., Yang, Z., Wu, X. & Hu, J. Effective model and pairing tendency in bilayer Ni-based superconductor  $\text{La}_3\text{Ni}_2\text{O}_7$  *arXiv* 2306.07275 (2023).
- [29] Shen, Y., Qin, M. & Zhang, G.-M. Effective bilayer model Hamiltonian and density-matrix renormalization group study for the high- $T_c$  superconductivity in  $\text{La}_3\text{Ni}_2\text{O}_7$  under high pressure *arXiv* 2306.07837 (2023).
- [30] Liu, Y.-B., Mei, J.-W., Ye, F., Chen, W.-Q. & Yang, F. The  $s_{\pm}$ -wave Pairing and the Destructive Role of Apical-Oxygen Deficiencies in  $\text{La}_3\text{Ni}_2\text{O}_7$  Under Pressure *arXiv* 2307.10144 (2023).
- [31] Lechermann, F., Gondolf, J., Bötzel, S. & Eremin, I. M. Electronic correlations and superconducting instability in  $\text{La}_3\text{Ni}_2\text{O}_7$  under high pressure *arXiv* 2306.05121 (2023).
- [32] Christiansson, V., Petocchi F. & Werner, P. Correlated electronic structure of  $\text{La}_3\text{Ni}_2\text{O}_7$  under pressure *arXiv* 2306.07931 (2023).
- [33] Shilenko D. A. & Leonov, I. V. Correlated electronic structure, orbital-selective behavior, and magnetic correlations in double-layer  $\text{La}_3\text{Ni}_2\text{O}_7$  under pressure *arXiv* 2306.14841 (2023).
- [34] Cao, Y. & Yang, Y.-F. Flat bands promoted by Hund's rule coupling in the candidate double-layer high-temperature superconductor  $\text{La}_3\text{Ni}_2\text{O}_7$  *arXiv* 2307.06806 (2023).
- [35] Liu, Z. *et al.* Electronic correlations and energy gap in the bilayer nickelate  $\text{La}_3\text{Ni}_2\text{O}_7$  *arXiv* 2307.02950 (2023).
- [36] Wu, W., Luo, Z., Yao, D.-X. & Wang, M. Charge Transfer and Zhang-Rice Singlet Bands in the Nickelate Superconductor  $\text{La}_3\text{Ni}_2\text{O}_7$  under Pressure *arXiv* 2307.05662 (2023).
- [37] Chen, X., Jiang, P., Li, J., Zhong, Z. & Lu, Y. Critical charge and spin instabilities in superconducting  $\text{La}_3\text{Ni}_2\text{O}_7$  *arXiv* 2307.07154 (2023).
- [38] Momma, K. & Izumi, F. Vesta 3 for three-dimensional visualization of crystal, volumetric and morphology data. *J. Appl. Crystallogr.* **44**, 1272-1276 (2011).
- [39] Orobengoa, D., Capillas, C., Aroyo, M. I. & Perez-Mato, J. M. AMPLIMODES: symmetry-mode analysis on the Bilbao Crystallographic Server *J. Appl. Crystallogr.* **42**, 820 (2009).
- [40] Perez-Mato, J., Orobengoa, D. & Aroyo, M. I. Mode crystallography of distorted structures *Acta Crystallogr. A* **66**, 558 (2010).
- [41] Baroni, S., Giannozzi, P. & Testa, A. Green's-function approach to linear response in solids *Phys. Rev. Lett.* **58**, 1861 (1987).
- [42] Gonze, X. Perturbation expansion of variational principles at arbitrary order *Phys. Rev. A* **52**, 1086 (1995).
- [43] Gonze, X. Adiabatic density-functional perturbation theory *Phys. Rev. A* **52**, 1096 (1995).
- [44] Chaput, L., Togo, A., Tanaka, I. & Hug, G. Phonon-phonon interactions in transition metals *Phys. Rev. B* **84**, 094302 (2011).
- [45] Togo, A. Tanaka, & I. First principles phonon calculations in materials science *Scr. Mater.* **108**, 1 (2015).
- [46] Hou, J. *et al.* Emergence of high-temperature superconducting phase in the pressurized  $\text{La}_3\text{Ni}_2\text{O}_7$  crystals *arXiv* 2307.09865 (2023).
- [47] Nakata, M., Ogura, D., Usui, H. & Kuroki, K. Finite-energy spin fluctuations as a pairing glue in systems with coexisting electron and hole bands *Phys. Rev. B* **95**, 214509 (2017).
- [48] Maier, T. A. & Scalapino, D. J. Pair structure and the pairing interaction in a bilayer Hubbard model for unconventional superconductivity *Phys. Rev. B* **84**, 180513(R) (2011).
- [49] Mishra, V., Maier, T. A. & Scalapino, D. J.  $s_{\pm}$  pairing near a Lifshitz transition *Sci Rep.* **6**, 32078 (2016).
- [50] Maier, T. A., Mishra, V., Balduzzi, G. & Scalapino, Ef-



- fective pairing interaction in a system with an incipient band *Phys. Rev. B* **99**, 140504(R) (2019).
- [51] Dee, P. M., Johnston, S. & Maier, T. A. Enhancing  $T_c$  in a composite superconductor/metal bilayer system: A dynamical cluster approximation study *Phys. Rev. B* **105**, 214502 (2022).
- [52] Mostofi, A. A. *et al.* Wannier90: A tool for obtaining maximally-localised wannier functions. *Comput. Phys. Commun.* **178**, 685-699 (2008).
- [53] Liechtenstein, A. I., Anisimov, V. I. & Zaanen, J. Density-functional theory and strong interactions: Orbital ordering in Mott-Hubbard insulators *Phys. Rev. B* **52**, R5467 (1995).
- [54] Lin, L.-F., Zhang, Y., Alvarez, G., Moreo, A. & Dagotto, E. Origin of insulating ferromagnetism in iron oxychalcogenide  $Ce_2O_2FeSe_2$ . *Phys. Rev. Lett.* **127**, 077204 (2021).
- [55] Fernandes, R. M., *et al.* Unconventional pairing in the iron arsenide superconductors. *Phys. Rev. B* **81**, 140501(R) (2010), and references therein. *Phys. Rev. B* **81**, 140501(R) (2010).
- [56] Liang, S., Moreo, A., Dagotto, & E., Nematic State of Pnictides Stabilized by Interplay between Spin, Orbital, and Lattice Degrees of Freedom. *Phys. Rev. Lett.* **111**, 047004 (2013), and references therein.
- [57] Kresse, G., & Hafner J. Ab initio molecular dynamics for liquid metals. *Phys. Rev. B* **47**, 558 (1993).
- [58] Kresse, G., & Furthmüller, J. Efficient iterative schemes for ab initio total-energy calculations using a plane-wave basis set. *Phys. Rev. B* **54**, 11169 (1996).
- [59] Blöchl, P. E. Projector augmented-wave method. *Phys. Rev. B* **50**, 17953 (1994).
- [60] Perdew, J. P., K. Burke, & Ernzerhof, M. Generalized Gradient Approximation Made Simple. *Phys. Rev. Lett.* **77**, 3865 (1996).
- [61] Dudarev, S. L., Botton, G. A., Savrasov, S. Y., Humphreys, C. J. & Sutton, A. P. Electron-energy-loss spectra and the structural stability of nickel oxide: An LSDA+U study *Phys. Rev. B* **57**, 1505 (1998).
- [62] Rømer, A. T., *et al.* Pairing in the two-dimensional Hubbard model from weak to strong coupling *Phys. Rev. Res.* **2**, 13108 (2020).
- [63] Kubo, K., Pairing symmetry in a two-orbital Hubbard model on a square lattice *Phys. Rev. B* **8**, 224509 (2007).
- [64] Graser, S., Maier, T. A., Hirschfeld, P. J., & Scalapino, D. J., Near-degeneracy of several pairing channels in multiorbital models for the Fe pnictides *New J. Phys.* **11**, 25016 (2009).
- [65] Altmeyer, M., *et al.* Role of vertex corrections in the matrix formulation of the random phase approximation for the multiorbital Hubbard model *Phys. Rev. B* **94**, 214515 (2016).
- [66] Maier, T. M., & Dagotto, E. Coupled Hubbard ladders at weak coupling: Pairing and spin excitations *Phys. Rev. B* **105**, 054512 (2022).

## Acknowledgements

The work was supported by the U.S. Department of Energy (DOE), Office of Science, Basic Energy Sciences (BES), Materials Sciences and Engineering Division.

## Author contributions

Y.Z., T.A.M., and E.D. designed the project. Y.Z. and L.-F. Lin carried out numerical calculations for DFT and the TB model. T.A.M. performed RPA calculations. Y.Z., A.M.,

T.A.M., and E.D. wrote the manuscript. All co-authors provided useful comments and discussion on the paper.

## Competing interests

The authors declare no competing interest.

## Additional information

**Supplementary information** The online version contains supplementary material available at [xx/xxxxxx](https://doi.org/10.1038/s41533-022-00000-0).

# Supplementary Material of “Structural phase transition, $s_{\pm}$ -wave pairing and magnetic stripe order in the bilayered nickelate superconductor $\text{La}_3\text{Ni}_2\text{O}_7$ under pressure”

Yang Zhang,<sup>1</sup> Ling-Fang Lin,<sup>1</sup> Adriana Moreo,<sup>1,2</sup> Thomas A. Maier,<sup>3</sup> and Elbio Dagotto<sup>1,2</sup>

<sup>1</sup>*Department of Physics and Astronomy, University of Tennessee, Knoxville, Tennessee 37996, USA*

<sup>2</sup>*Materials Science and Technology Division, Oak Ridge National Laboratory, Oak Ridge, Tennessee 37831, USA*

<sup>3</sup>*Computational Sciences and Engineering Division,*

*Oak Ridge National Laboratory, Oak Ridge, Tennessee 37831, USA*

(Dated: August 3, 2023)

## I. SUPPLEMENTARY NOTE I: PHONON SPECTRUM UNDER PRESSURE

We calculated the phonon spectrum of the Fmmm and Amam phases of  $\text{La}_3\text{Ni}_2\text{O}_7$  for different pressures, by using the density functional perturbation theory approach [1–3] analyzed by the PHONOPY software [4, 5]. The phonon dispersion spectra clearly display imaginary frequencies at high symmetry points for the Fmmm structure of LNO below 10.5 Gpa, while the Fmmm phase becomes stable without any imaginary frequency from 10.6 Gpa to 50 Gpa, the maximum value we studied, as shown in Fig. S1 and Fig. S2. For the Amam phase of LNO, there is no imaginary frequency obtained in the phonon dispersion spectra, indicating that the Amam phase is stable from 0 to 14 Gpa (see Fig. S3).

## II. SUPPLEMENTARY NOTE II: HOPPINGS AND FERMI SURFACE UNDER PRESSURE

Based on the hoppings and crystal-field splitting obtained from the maximally localized Wannier functions [6], we calculated the Fermi surfaces for different pressures (see Fig. S4), by using a bilayer four-band  $e_g$ -orbital tight binding (TB) model with nearest-neighbor (NN) hopping (see Fig. S5). The Fermi level is made of two pockets ( $\alpha$  and  $\beta$ ) with a mixture of  $d_{3z^2-r^2}$  and  $d_{x^2-y^2}$  orbitals, while the  $\gamma$  pocket is made almost exclusively of the  $d_{3z^2-r^2}$  orbital.

Below is the list of hopping amplitudes for the Fmmm phase at several pressures, deduced from DFT bands and the fitting near the Fermi level using a tight-binding two-orbital model. The values at 0 Gpa and 50 Gpa can be found in the main text. Varying pressure, the hoppings only weakly change.

### A. Hoppings at 5 Gpa

$$t_{\bar{x}} = \begin{bmatrix} d_{z^2} & d_{x^2-y^2} \\ -0.094 & 0.216 \\ 0.216 & -0.468 \end{bmatrix}, \quad (\text{S3})$$

$$t_{\bar{y}} = \begin{bmatrix} d_{z^2} & d_{x^2-y^2} \\ -0.094 & -0.216 \\ -0.216 & -0.468 \end{bmatrix}, \quad (\text{S4})$$

$$t_{\bar{z}} = \begin{bmatrix} d_{z^2} & d_{x^2-y^2} \\ -0.611 & 0.000 \\ 0.000 & 0.000 \end{bmatrix}. \quad (\text{S5})$$

### B. Hoppings at 10 Gpa

$$t_{\bar{x}} = \begin{bmatrix} d_{z^2} & d_{x^2-y^2} \\ -0.097 & 0.224 \\ 0.224 & -0.480 \end{bmatrix}, \quad (\text{S6})$$

$$t_{\bar{y}} = \begin{bmatrix} d_{z^2} & d_{x^2-y^2} \\ -0.097 & -0.224 \\ -0.224 & -0.480 \end{bmatrix}, \quad (\text{S7})$$

$$t_{\bar{z}} = \begin{bmatrix} d_{z^2} & d_{x^2-y^2} \\ -0.625 & 0.000 \\ 0.000 & 0.000 \end{bmatrix}. \quad (\text{S8})$$

### C. Hoppings at 15 Gpa

$$t_{\bar{x}} = \begin{bmatrix} d_{z^2} & d_{x^2-y^2} \\ -0.100 & 0.230 \\ 0.230 & -0.490 \end{bmatrix}, \quad (\text{S9})$$

$$t_{\bar{y}} = \begin{bmatrix} d_{z^2} & d_{x^2-y^2} \\ -0.100 & -0.230 \\ -0.230 & -0.490 \end{bmatrix}, \quad (\text{S10})$$

$$t_{\bar{z}} = \begin{bmatrix} d_{z^2} & d_{x^2-y^2} \\ -0.640 & 0.000 \\ 0.000 & 0.000 \end{bmatrix}. \quad (\text{S11})$$

### D. Hoppings at 20 Gpa

$$t_{\bar{x}} = \begin{bmatrix} d_{z^2} & d_{x^2-y^2} \\ -0.106 & 0.238 \\ 0.238 & -0.505 \end{bmatrix}, \quad (\text{S12})$$

$$t_{\bar{y}} = \begin{bmatrix} d_{z^2} & d_{x^2-y^2} \\ -0.106 & -0.238 \\ -0.238 & -0.505 \end{bmatrix}, \quad (\text{S13})$$

$$t_{\bar{z}} = \begin{bmatrix} d_{z^2} & d_{x^2-y^2} \\ -0.654 & 0.000 \\ 0.000 & 0.000 \end{bmatrix}. \quad (\text{S14})$$

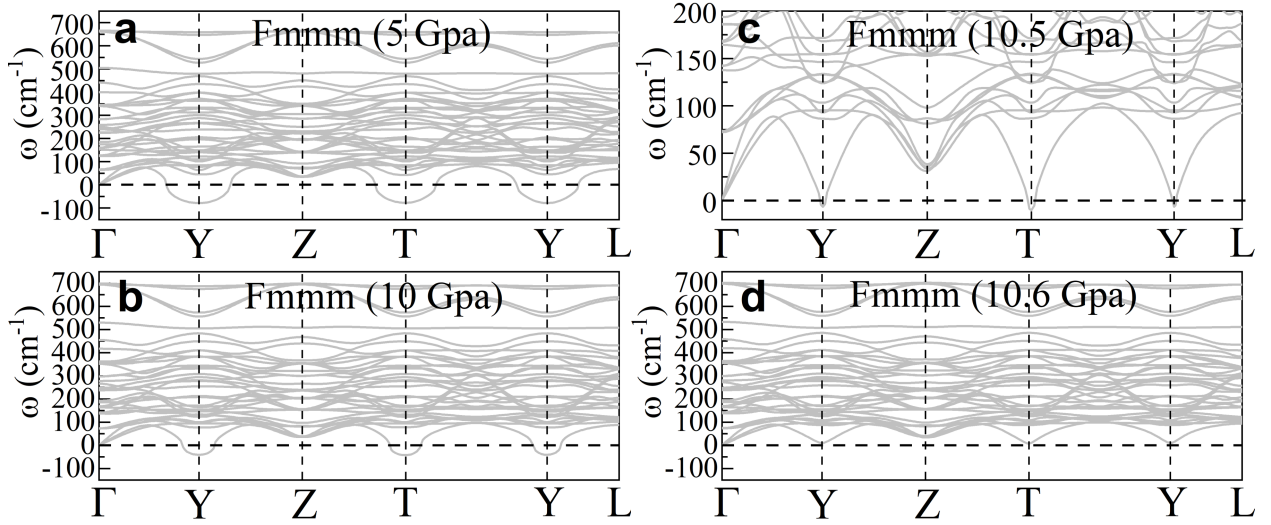


FIG. S1. **Phonon spectrum of the Fmmm phase under pressure.** Phonon spectrum of LNO for the Fmmm (No. 69) phase at **a** 5 Gpa, **b** 10 Gpa, **c** 10.5 Gpa, and **d** 10.6 Gpa, respectively. For the Fmmm phase, the coordinates of the high-symmetry points in the Brillouin zone (BZ) are  $\Gamma = (0, 0, 0)$ ,  $Y = (0.5, 0, 0.5)$ ,  $Z = (0.5, 0.5, 0)$ ,  $T = (0, 0.5, 0.5)$ , and  $L = (0.5, 0.5, 0.5)$ .

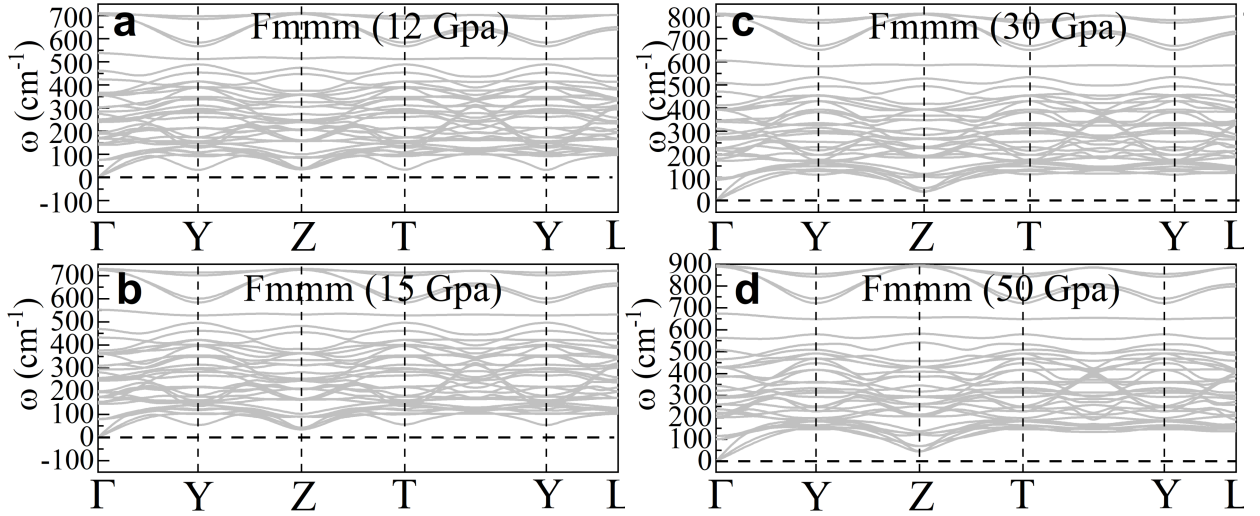


FIG. S2. **Phonon spectrum of the Fmmm phase under pressure.** Phonon spectrum of LNO for the Fmmm (No. 69) phase at **a** 12 Gpa, **b** 15 Gpa, **c** 30 Gpa, and **d** 50 Gpa, respectively. For the Fmmm phase, the coordinates of the high-symmetry points in the BZ are  $\Gamma = (0, 0, 0)$ ,  $Y = (0.5, 0, 0.5)$ ,  $Z = (0.5, 0.5, 0)$ ,  $T = (0, 0.5, 0.5)$ , and  $L = (0.5, 0.5, 0.5)$ .

### E. Hoppings at 25 Gpa

$$t_{\bar{x}} = \begin{bmatrix} d_{z^2} & d_{x^2-y^2} \\ -0.110 & 0.243 \\ 0.243 & -0.515 \end{bmatrix}, \quad (\text{S15})$$

$$t_{\bar{y}} = \begin{bmatrix} d_{z^2} & d_{x^2-y^2} \\ -0.110 & -0.243 \\ -0.243 & -0.515 \end{bmatrix}, \quad (\text{S16})$$

$$t_{\bar{z}} = \begin{bmatrix} d_{z^2} & d_{x^2-y^2} \\ -0.666 & 0.000 \\ 0.000 & 0.000 \end{bmatrix}. \quad (\text{S17})$$

### F. Hoppings at 30 Gpa

$$t_{\bar{x}} = \begin{bmatrix} d_{z^2} & d_{x^2-y^2} \\ -0.113 & 0.250 \\ 0.250 & -0.526 \end{bmatrix}, \quad (\text{S18})$$

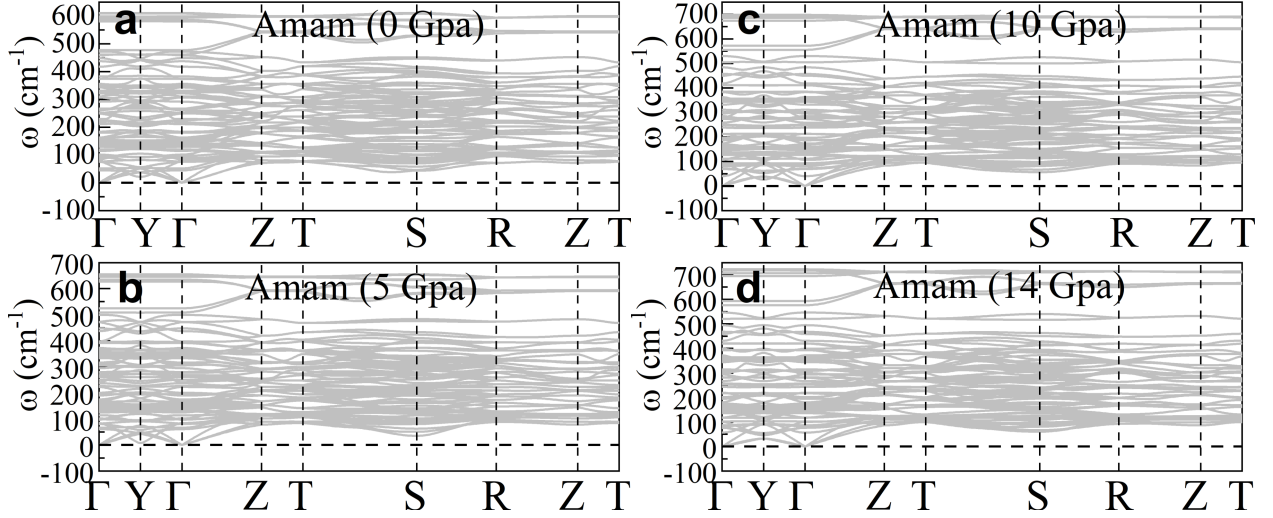


FIG. S3. **Phonon spectrum of the Amam phase under pressure.** Phonon spectrum of LNO for the Fmmm (No. 69) phase at **a** 0 Gpa, **b** 5 Gpa, **c** 10 Gpa, and **d** 14 Gpa, respectively. For the Amam phase, the coordinates of the high-symmetry points in the BZ are  $\Gamma = (0, 0, 0)$ ,  $Y = (0.5, 0, 0.5)$ ,  $Z = (0.5, 0.5, 0)$ ,  $T = (0, 0.5, 0.5)$ , and  $L = (0.5, 0.5, 0.5)$ .

$$t_{\bar{y}} = \begin{bmatrix} d_{z^2} & d_{x^2-y^2} \\ -0.113 & -0.250 \\ -0.250 & -0.526 \end{bmatrix}, \quad (\text{S19})$$

$$t_{\bar{z}} = \begin{bmatrix} d_{z^2} & d_{x^2-y^2} \\ -0.676 & 0.000 \\ 0.000 & 0.000 \end{bmatrix}. \quad (\text{S20})$$

### G. Hoppings at 35 Gpa

$$t_{\bar{x}} = \begin{bmatrix} d_{z^2} & d_{x^2-y^2} \\ -0.116 & 0.256 \\ 0.256 & -0.534 \end{bmatrix}, \quad (\text{S21})$$

$$t_{\bar{y}} = \begin{bmatrix} d_{z^2} & d_{x^2-y^2} \\ -0.116 & -0.256 \\ -0.256 & -0.534 \end{bmatrix}, \quad (\text{S22})$$

$$t_{\bar{z}} = \begin{bmatrix} d_{z^2} & d_{x^2-y^2} \\ -0.686 & 0.000 \\ 0.000 & 0.000 \end{bmatrix}. \quad (\text{S23})$$

### H. Hoppings at 40 Gpa

$$t_{\bar{x}} = \begin{bmatrix} d_{z^2} & d_{x^2-y^2} \\ -0.118 & 0.260 \\ 0.260 & -0.540 \end{bmatrix}, \quad (\text{S24})$$

$$t_{\bar{y}} = \begin{bmatrix} d_{z^2} & d_{x^2-y^2} \\ -0.118 & -0.260 \\ -0.260 & -0.540 \end{bmatrix}, \quad (\text{S25})$$

$$t_{\bar{z}} = \begin{bmatrix} d_{z^2} & d_{x^2-y^2} \\ -0.696 & 0.000 \\ 0.000 & 0.000 \end{bmatrix}. \quad (\text{S26})$$

### I. Hoppings at 45 Gpa

$$t_{\bar{x}} = \begin{bmatrix} d_{z^2} & d_{x^2-y^2} \\ -0.121 & 0.263 \\ 0.263 & -0.546 \end{bmatrix}, \quad (\text{S27})$$

$$t_{\bar{y}} = \begin{bmatrix} d_{z^2} & d_{x^2-y^2} \\ -0.121 & -0.263 \\ -0.263 & -0.546 \end{bmatrix}, \quad (\text{S28})$$

$$t_{\bar{z}} = \begin{bmatrix} d_{z^2} & d_{x^2-y^2} \\ -0.706 & 0.000 \\ 0.000 & 0.000 \end{bmatrix}. \quad (\text{S29})$$

## III. SUPPLEMENTARY NOTE III: ADDITIONAL DFT MAGNETIC STATES RESULTS

Here, we considered three possible in-plane spin orders: A-AFM with wavector  $(0,0)$ , G-AFM with  $(\pi, \pi)$ , and stripe with  $(\pi, 0)$  orders in plane, while the magnetic coupling between layers was considered to be AFM in all cases, using

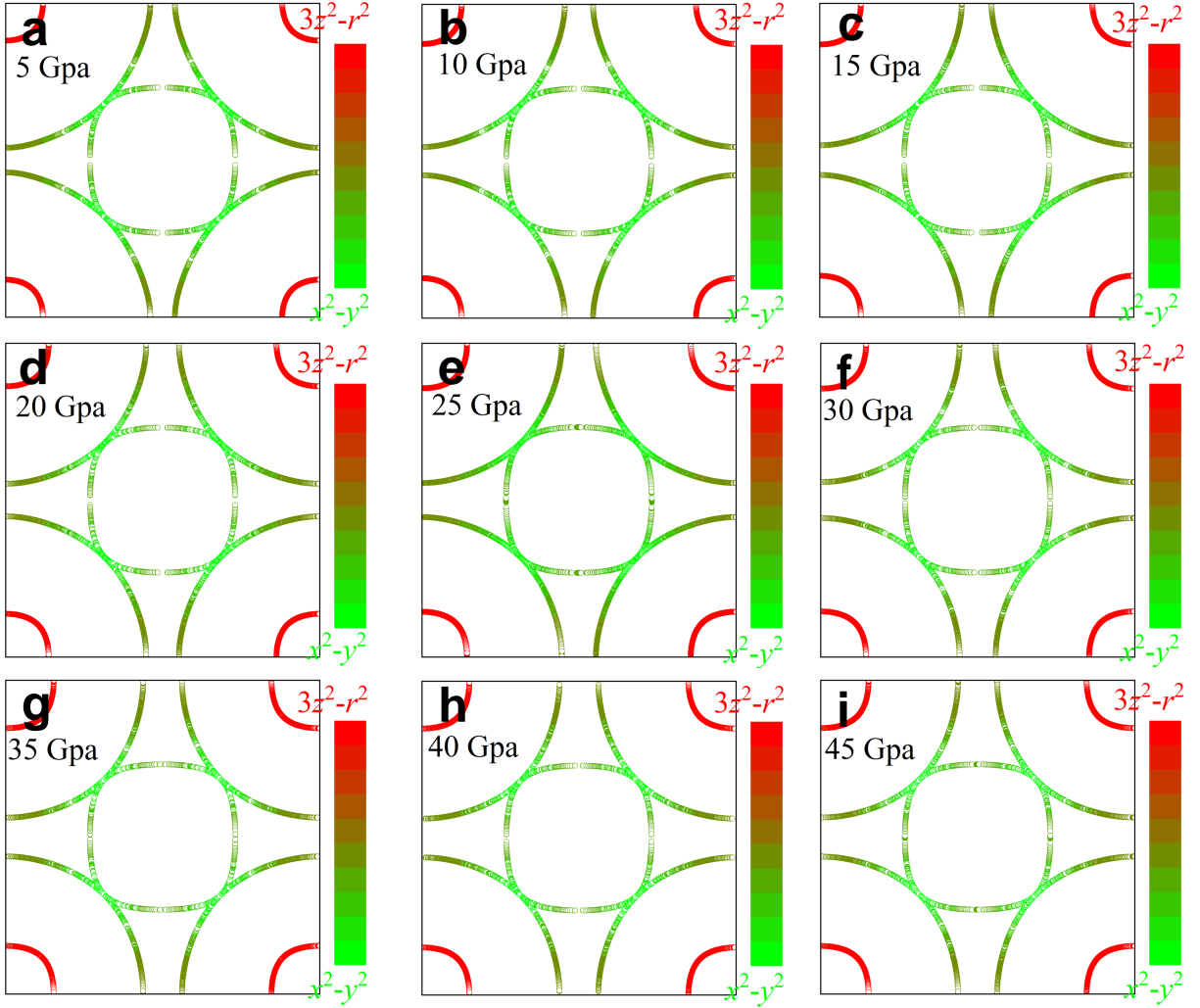


FIG. S4. Evolution of the Fermi surface under pressure in the Fmmm phase and in the non-superconducting regime. **a-i** Fermi surfaces from 5 and 45 Gpa obtained from TB calculations. Here, the four-band  $e_g$ -orbital TB model was used, with NN hoppings in a bilayer lattice for the overall filling  $n = 3$  (1.5 electrons per site). **a** 5 Gpa, **b** 10 Gpa, **c** 15 Gpa, **d** 20 Gpa, **e** 25 Gpa, **f** 30 Gpa, **g** 35 Gpa, **h** 40 Gpa, and **i** 45 Gpa, respectively.

the optimized crystal structures at different pressures. Then, the differences in total energy and enthalpy between different magnetic configurations are the same due to having the same crystal structures at different pressures.

As shown in Fig. S6, by *decreasing* the Hund coupling in units of  $U$  as compared with values used in the main text, namely by using  $J = 0.4$  eV and  $U = 4$  eV, the G-type AFM order now becomes the lowest energy state as pressure increases instead of the stripe magnetic order, due to the enhanced antiferromagnetic Heisenberg interaction induced by the larger intraorbital hopping under pressure. This highlights that the stripe order, and associated  $s^\pm$  pairing, is stable when the Hund coupling is robust.

The calculated magnetic moments of different magnetic phases they all decrease when increasing pressure, as shown in Fig. S7.

#### IV. SUPPLEMENTARY NOTE IV: IMPORTANCE OF M POINT POCKET

To better understand the importance of the  $\gamma$  pocket in the pairing process, we calculated the Fermi surface by changing the  $\Delta$  to 0.6 eV, while other parameters remain the same as for 0 Gpa. The hole band sinks below the Fermi level and the  $\gamma$ -pocket disappears, as shown in Fig. S8. The most notorious aspect to notice is that the pockets at  $(\pi, \pi)$ , and rotated equivalent points, are absent. This goes together with the suppression of  $s^\pm$  pairing.

[1] Baroni, S., Giannozzi, P. & Testa, A. Green's-function approach to linear response in solids *Phys. Rev. Lett.* **58**,

1861 (1987).

Ni bilayer lattice

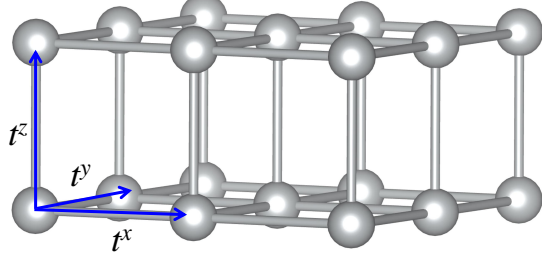


FIG. S5. (b) **Sketch of the Ni bilayer lattice.** Sketch of the Ni bilayer lattice structure used in the TB model with NN hopping.

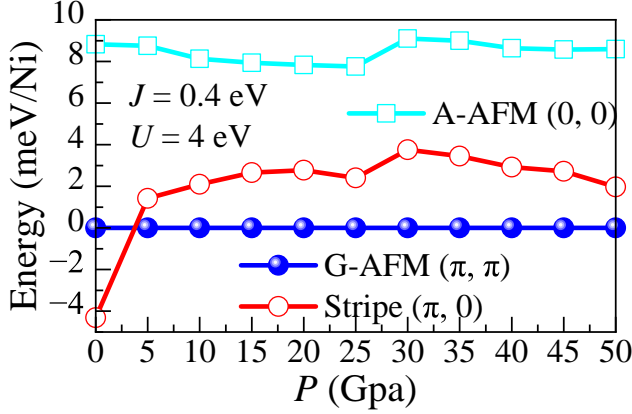


FIG. S6. **Magnetic results at  $J = 0.4$  eV.** The DFT calculated energies for  $J = 0.4$  eV corresponding to different magnetic configurations vs different values of pressure, at  $U = 4$  eV.

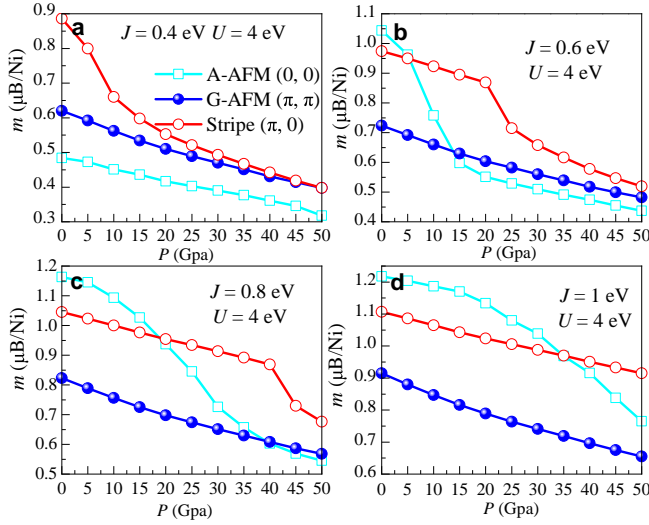


FIG. S7. **The calculated magnetic moments under pressure.** The DFT calculated magnetic moments for **a**  $J = 0.4$  eV, **b**  $J = 0.6$  eV, **c**  $J = 0.8$  eV, and **d**  $J = 1$  eV for different magnetic configurations vs different values of pressure, all at  $U = 4$  eV, respectively.

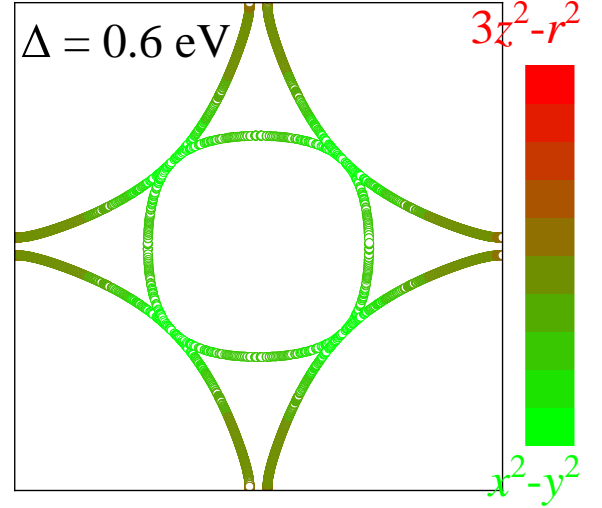


FIG. S8. **The Fermi surface with  $\Delta = 0.6$  eV.** Fermi surfaces for  $\Delta = 0.6$  eV from TB calculations. Here, the hopping matrix for 0 Gpa was used. Specifically, the hoppings used are:  $t_{11}^x = t_{11}^y = -0.088$ ,  $t_{12}^x = 0.208$ ,  $t_{12}^y = -0.208$ ,  $t_{22}^x = t_{22}^y = -0.455$ , and  $t_{11}^z = -0.603$ . All the hoppings are in eV units. Note the absence of the pocket at  $(\pi, \pi)$  due to the increase in  $\Delta$ , which also causes the  $s^\pm$  pairing to stop dominating over  $d$ -wave, see main text.

- [2] Gonze, X. Perturbation expansion of variational principles at arbitrary order *Phys. Rev. A* **52**, 1086 (1995).
- [3] Gonze, X. Adiabatic density-functional perturbation theory *Phys. Rev. A* **52**, 1096 (1995).
- [4] Chaput, L., Togo, A., Tanaka, I. & Hug, G. Phonon-phonon interactions in transition metals *Phys. Rev. B* **84**, 094302 (2011).
- [5] Togo, A. Tanaka, & I. First principles phonon calculations in materials science *Scr. Mater.* **108**, 1 (2015).
- [6] Mostofi, A. A. *et al.* Wannier90: A tool for obtaining maximally-localised wannier functions. *Comput. Phys. Commun.* **178**, 685-699 (2008).